Garnet, the archetypal cubic mineral, does not grow cubic

Cesare B.[1*], Nestola F.[1], Johnson T.[2], Mugnaioli E.[3], Della Ventura G.[4,5], Peruzzo L.[6], Bartoli O.[1], Viti C.[7], Erickson T.[8]

1) Dipartimento di Geoscienze, Università degli Studi di Padova, via Gradenigo 6, 35131 Padova, Italy
2) School of Earth and Planetary Sciences, Curtin University, Bentley 6102, Perth, Australia
3) Center for Nanotechnology Innovation@NEST, Istituto Italiano di Tecnologia, Piazza San Silvestro 12, 56127 Pisa, Italy
4) Dipartimento di Scienze, Università di Roma Tre, Largo San Leonardo Murialdo 1, 00146 Rome, Italy
5) Istituto Nazionale di Fisica Nucleare, Via Enrico Fermi 40, 00044 Frascati, Italy
6) Istituto di Geoscienze e Georisorse, CNR, via Gradenigo 6, 35131, Padova, Italy
7) Dipartimento di Scienze Fisiche, della Terra e dell'Ambiente, Università di Siena
8) Jacobs – JETS, NASA Johnson Space Center, Astromaterials Research and Exploration Science Division, Mailcode XI3, 2101 NASA Parkway, Houston, TX, 77058 USA

*) corresponding author: bernardo.cesare@unipd.it

Abstract

Garnet is the archetypal cubic mineral, occurring in a wide variety of rock types in Earth's crust and upper mantle. Owing to its prevalence, durability and compositional diversity, garnet is used to investigate a broad range of geological processes. Although birefringence is a characteristic feature of rare Ca–Fe^{3+} garnet and Ca-rich hydrous garnet, the optical anisotropy that has occasionally been documented in common (that is, anhydrous Ca–Fe^{2+}–Mg–Mn) garnet is generally attributed to internal strain of the cubic structure. Here we show that common garnet with a non-cubic (tetragonal) crystal structure is much more widespread than previously thought, occurring in low-temperature, high-pressure metamorphosed basalts (blueschists) from subduction zones and in low-grade metamorphosed mudstones (phyllites and schists) from orogenic belts. Indeed, a non-cubic symmetry appears to be typical of common garnet that forms at low temperatures (<450°C), where it has a characteristic Fe–Ca-rich composition with very low Mg contents. We propose that, in most cases garnet does not initially grow cubic. Our discovery indicates that the crystal chemistry and thermodynamic properties of garnet at low-temperature need to be re-assessed, with potential consequences for the application of garnet as an investigative tool in a broad range of geological environments.

Introduction

Garnet is one of the most widely occurring minerals in the Earth. It is stable to temperatures (*T*) approaching 2000°C and pressures (*P*) of ~25 GPa, and occurs in broad variety of rock compositions ranging from mantle peridotite to metamorphosed basalt, granite and mudstone[1]. Owing to its prevalence, durability and compositional diversity, including the ability to preferentially incorporate particular trace elements and isotopes, garnet is one of the most useful minerals for investigating a wide range of fundamental geological processes. These include estimating the *P*–*T* evolution and oxygen fugacity of rocks[2,3,4,5], constraining volatile fluxes in the crust and mantle[6,7], determining the absolute timing and rates of geological processes[8,9], assessing the rheological properties of the lithosphere[10], constraining the geodynamic setting of magmatic and metamorphic systems[11,12], and tracking individual earthquake cycles[13].

Garnet has the general formula $X_3Y_2(SiO_4)_3$[14,15]. In almost all metamorphosed crustal rocks in which it occurs, the composition of garnet lies between the end members pyrope [$Mg_3Al_2(SiO_4)_3$],

almandine [$Fe^{2+}_3Al_2(SiO_4)_3$], spessartine [$Mn_3Al_2(SiO_4)_3$] and grossular [$Ca_3Al_2(SiO_4)_3$)][16]. Such 'common' garnet, which is anhydrous, typically has a cubic structure (space group *Ia*-3*d*) and is optically isotropic[15]. Much rarer are the so-called grandite garnet, a solid solution between grossular and andradite [$Ca_3Fe^{3+}_2(SiO_4)_3$], and hydrogrossular garnet [$Ca_3Al_2(SiO_4)_{3-x}(H_4O_4)_x$]. These unusual compositions typically exhibit optical birefringence that is accompanied by oscillatory or sector zoning. In these cases, the birefringence is either related to a departure from cubic symmetry[17,18], or to intergrowths with structural mismatches that induce lattice strain[19].

Birefringence has rarely been noted in common garnet[20]. In such cases, the anisotropy has been attributed to either externally-imposed strain or internal lattice strain, the latter due to the size difference between larger Ca cations and smaller Fe, Mg or Mn cations in the *X* site of the structure[20]. In one case, this mismatch has been interpreted to produce partial long-range ordering and, based on X-ray single-crystal diffraction, a tetragonal symmetry has been proposed for a common garnet from an eclogite[21]. For this sample, however, the differences in the refined unit-cell parameters were too small to unambiguously demonstrate a non-cubic symmetry.

Here we demonstrate that the commonly accepted view that a tetragonal symmetry is restricted to some grandite and hydro- (or fluoro-) garnet compositions[15] is wrong. Using some spectacular natural samples of garnet-bearing high-pressure, low temperature metamorphosed basalt (blueschist) exhumed from subduction zones and greenschist-facies metamorphosed mudstones (phyllites) from the roots of mountain ranges, and utilising a multi-technique approach including optical microstructural analysis, BSEM, EMPA, EBSD, FTIR, TEM and single-crystal XRD, we show that common garnet in these low-temperature regional metamorphic rocks[16] initially grows as a tetragonal, not cubic, mineral.

Results

Petrography of tetragonal garnet

Garnet exhibiting optical birefringence is common in samples of blueschist from the Franciscan mélange, California[22] (specifically at the Cazadero and Jenner localities) and from Corsica (the Marine de Farinole locality) and in phyllites and micaschists from the central and eastern Italian Alps (namely at Maniva pass, Pfitscher Joch and a third unspecified locality) (Fig. 1, 2; Supplementary Fig. S1, Supplementary Videos S1-S4 online). The Cazadero blueschist has a very simple mineralogy,

consisting of sodic amphibole, garnet, pyrite and quartz, with accessory apatite and allanite. Garnet porphyroblasts form euhedral to partly resorbed crystals up to 1.5 mm in diameter, having inclusion-rich cores. The blueschist from Jenner contains euhedral, fractured porphyroblasts of garnet up to 3 mm in diameter, set in a weakly-foliated matrix composed mainly of glaucophane with minor quartz, chlorite, phengite and titanite. At Farinole, Corsica, birefringent garnet is associated with glaucophane, zoisite, relict omphacite, rutile, ilmenite, titanite and retrograde chlorite. The garnet is euhedral, up to 3 mm in diameter, commonly fractured, and may contain inclusions of glaucophane. The sample from Maniva pass is a fine-grained muscovite–chlorite–albite–quartz phyllite, with scarce biotite and abundant garnet <0.4 mm in diameter that is partially replaced by chlorite. The sample from Pfitscher Joch is a biotite–muscovite–chlorite schist with euhedral garnet porphyroblasts up to 3 mm in diameter. It contains epidote but no plagioclase. The sample from the eastern Alps is a chlorite-rich, biotite-free, muscovite–albite phyllite containing euhedral garnet (<3 mm across) that shows only very limited replacement by chlorite.

The Cazadero blueschists equilibrated at temperatures of less than 350°C and pressures between 0.5 and 0.9 GPa [23,24]. The studied sample lacks omphacite, and it is likely that these rocks never experienced higher temperatures[25]. Given the anticlockwise metamorphic evolution proposed for the Franciscan rocks in the area[26], the Jenner blueschists probably record temperatures close to 400°C and pressures in excess of 1.0 GPa. The Farinole blueschists record temperatures of 400–500°C and pressures of 0.7–0.9 GPa during a blueschist-facies event that postdated eclogite-facies metamorphism[27]. The mineral assemblage of the phyllites from Maniva and the eastern Alps suggests metamorphic conditions in the lower greenschist facies (T < 450°C). Conversely, the schist from Pfitscher Joch reached lower amphibolite-facies conditions of 520 ± 30°C and 0.65 ± 0.1 GPa [28].

In the Cazadero sample, birefringence is apparent in conventional 30 μm thin sections in crossed polarised light, but in the samples from the other cases it is so weak that it is easily overlooked. In those instances, the use of thicker sections of 100 μm reveals patterns of birefringence (Fig. 2a. Supplementary Fig. S1 online). Optical sector zoning[29] is the most striking optical evidence of birefringence (Fig. 1, 2 a–d; Supplementary Fig. S2 and Videos S1–S3 online), which is most clearly developed in garnet from the Cazadero blueschist[30] and in the phyllites from the eastern Alps and Pfitscher Joch. The sector zoning appears to follow a rhombdodecahedral or combined icositetrahedral–rhombdodecahedral pattern[31]. The boundary between the sectors is sharp and

outlined by a thin black line in crossed polarized light (Fig. 1; 2 e, f), but is invisible in plane polarized light.

Irregular mottled birefringence is additionally developed in garnets that show sector zoning, but also in grains that do not. The best examples, preserved in the Jenner and Farinole blueschists and in the Pfitscher Joch micaschist, comprise thin stripes (layers in three dimensions) with a thickness up to a few tens of micrometers. The stripes are either straight or slightly curved and anastomosing and are typically arranged in two orientations that intersect at a high angle (Fig. 2f, g, Supplementary Fig. S1, Supplementary Video S4 online). A third mode of optical birefringence is evident as thin concentric oscillatory zoning, which occurs in garnets within the Cazadero blueschist (Fig. 1, 2b).

The chemical composition of tetragonal garnet

The major element chemical composition of the garnets varies among samples, with most showing core–rim zonation (Fig. 3; Supplementary Fig. S2 and Tab. S1 online). In all samples garnet is dominated by the almandine component (>58 mol.%) and contains significant amount of grossular (18–33 mol.%), variable spessartine (<22%) and very low pyrope (1–9%). Only the rim of the Pfitscher Joch sample departs from this compositional range, containing only 12 mol% grossular and 11 mol.% pyrope. A pronounced to weak bell-shaped distribution of Mn, in particular in the Cazadero and Farinole blueschists (Fig. 3a; Supplementary Fig. S2 online), is consistent with the preservation of growth zoning, and these garnets also preserve concentric oscillatory zoning towards the rim. Comparison of the patterns of chemical zoning and optical sector zoning reveals that the two are unrelated–that is, the boundaries of the optical sectors do not correspond to chemical discontinuities.

The oscillatory zoning at the rims of garnet involves primarily Fe^{2+} and Ca (Fig. 3a, c) that vary antithetically by up to 5 mol.% whereby the combined concentration of almandine and grossular remains constant. Most importantly, direct exchange of Ca for Fe^{2+} is also observed in portions of crystals devoid of optical oscillatory zoning, appearing as zones of mottled birefringence (Fig. 3b, c). Chemical profiles across these zones (Fig. 3c) indicate an almost perfect antithetic coupling between Ca and Fe^{2+}, in which concentrations of these components vary by up to 3 mol.% over distances of up to a few tens of micrometres. This suggests that the mottled birefringence may be related to an inhomogeneous distribution of Ca and Fe. The same pattern of antithetic variations in Ca and Fe^{2+} is

observed also in the core of a garnet from the Cazadero blueschist. The oscillatory zoning observed at Cazadero, involving essentially a $CaFe_{-1}$ exchange, is different from the rhythmic zoning in Mg and Mn that is commonly developed in other garnets from subduction zone environments and which is considered to track changes in pressure, in some cases reflecting earthquakes cycles[13]. In the blueschist garnets studied here, the Mg content is constant and very low. The birefringent garnet grains have compositions peculiar to blueschist-facies rocks[16] and very low-grade phyllites[32,33], defining a narrow compositional field with the lowest Mg/Ca values measured in metasedimentary and metabasic rocks (Fig. 4).

As birefringence in garnet may be related to the presence of OH or H_2O in the structure[14], we analysed the sector-zoned garnets from Cazadero, the eastern Alps and Pfitscher Joch by FTIR imaging, collecting both single-spots maps and FPA (focal-plane-array of detectors) images (Fig. 5). The results show that, although garnet in the Cazadero sample contains 100–300 μm-long needles and lamellae of hydroxylated minerals including chlorite, deerite, stilpnomelane, and phengite, the garnet itself is anhydrous within the limits of the technique (few ppm; Fig. 5c). Similarly, in the two phyllite samples, the garnet is OH-free, and the OH signal in the FTIR images is clearly associated with inclusions of phyllosilicates (Supplementary Fig. S3 online).

Constraints on crystal structure

Garnet crystals from five samples were characterized by single-crystal X-ray diffraction to collect complete intensity and structural data (see Methods). In all samples the systematic absences and the statistical analysis of the intensities are consistent with a tetragonal structure with $I4_1/acd$ space group (Supplementary Tab. S2 online). The difference between a,b and c cell edges is 17 to 35 times the experimental uncertainty. In the sample from Pfitscher Joch this difference is smaller, but still five times larger than the uncertainty.

A birefringent garnet from the Farinole blueschist was also investigated by an alternative single-crystal XRD technique that is both more precise and more accurate (see Methods). The data (45 different reflections each measured in eight different positions) confirm the tetragonal symmetry with $a = b = 11.6064(4)$ Å, $c = 11.6146(4)$ Å, and a unit cell volume of 1564.59(14) $Å^3$, in which the difference between *a*,*b* and *c* edges is more than ten times the experimental uncertainty

150 (Supplementary Tab. S2 online). The XRD data do not indicate any site preference among Fe, Ca, Mn
151 and Mg within the X1 and X2 sites.
152 The single-crystal XRD results are supported by electron diffraction tomography (EDT)
153 experiments. Reconstructed diffraction volumes from seven areas from a garnet from the Cazadero
154 blueschist show a pseudo-cubic cell with an identical orientation. However, in all cases one of the
155 main cell vectors is systematically longer than the average value by an amount comparable to the
156 EDT uncertainties (~2%) on cell parameters. This difference persists after the sample was rotated by
157 90°, excluding the possibility for experimental errors associated with the mechanical and optical
158 alignment of the TEM. Thus, the EDT intensity distributions confirm a tetragonal symmetry. Moreover,
159 violations on extinction conditions are observed in the reconstructed 3D diffraction volume, consistent
160 with space group $I4_1/a$ (Fig. 6a; Supplementary Fig. S4 online). Ab-initio structure solution was
161 achieved in space groups Ia-3d, $I4_1/acd$ and $I4_1/a$. A tentative refinement of the distribution of Ca and
162 Fe provided no evidence for short-range ordering.
163 Investigations using high-resolution transmitted electron microscopy (HRTEM) were
164 performed mostly in the [111] orientation, but crystals were also tilted in order to highlight any TEM
165 contrast and, thereby, assess any evidence for strain, twinning and structural defects. All garnets
166 display a homogeneous, ordered and undeformed crystal structure, with very limited strain or defects.
167 Selected area electron diffraction (SAED) patterns show intense and sharp reflections, with no
168 evidence for spot splitting or streaking. Rarely, the ordered crystal structure displays isolated planar
169 features (Fig. 6b) that may be consistent with the occurrence of twinning.
170 Electron Backscatter diffraction (EBSD) mapping of garnet from the Cazadero blueschist does
171 not reveal any significant microstructures that correlate with the observed optical sector zoning. This
172 suggests that the diffraction patterns are equivalent across the sector boundaries, and that boundaries
173 are merohedral twin planes[34]. At the micrometre scale, the grains are nominally undeformed with
174 intragranular misorientation <2.5° across grains that are >600 μm in diameter. While minor
175 misorientation is revealed in both the texture component and grain rotation hypermaps (Fig. 7;
176 Supplementary Fig. S5 online), the close correlation between the misorientations with chemical
177 variations resulting from the energy dispersive X-ray maps suggests that this is an artefact caused by
178 chemically-controlled shifts in the *d* spacing rather than by true structural defects.
179

Discussion

Our results clearly demonstrate the tetragonal nature of anhydrous Ca- and Fe^{2+}-rich common garnet in the blueschists and phyllites investigated as part of this study. It may be argued whether these are exceptional features occurring in local and/or unusual environments or, rather, whether they are representative of the general behaviour of low-temperature metamorphic settings. We favour the latter interpretation for the following reasons: i) we have analysed samples from six widely-distributed geographical localities and which occur in well-known and diverse geological setting (the Franciscan complex, Alpine Corsica, the Southalpine and Austroalpine domains of the Alps); ii) we randomly chose our samples from these low-grade metamorphic complexes, and; iii) all other blueschists from Farinole contain optically sector-zoned garnets, regardless of their precise bulk composition. In this respect, it is striking that birefringent, twinned garnet was observed in lithologically-diverse samples at Cazadero, including metachert, meta-ironstone and metacarbonate[30]. Birefringent garnet is also present in the schists of the Sambagawa metamorphic belt, Japan (O. Weller, personal communication), and in the lawsonite–epidote blueschists of the Sivrihisar Massif, Turkey (D. Whitney, personal communication). In both occurrences[35, 36] the garnet has the grossular-rich (~25 mol%), pyrope-poor (<7 mol%) composition that typifies the samples documented here.

In summary, a conclusion of the general applicability of the tetragonal nature of anhydrous common garnet in low-temperature metamorphic settings appears justified, and represents a hypothesis that is readily testable. Notably, there are no other studies demonstrating that common garnet from low-temperature metamorphic rocks and with a composition similar to those reported here are optically isotropic and have a cubic structure. We maintain that the non-cubic nature of these garnets has been overlooked because of the extremely low birefringence, whose detection is precluded in most cases due to examination of standard thin sections (0.030 mm) using a normal petrographic microscope[20]. We suggest that the use of thicker sections will reveal many more examples of birefringent, non-cubic garnets in low-grade metamorphic rocks worldwide.

We also suggest that garnet initially grows as a tetragonal mineral in most low-temperature metamorphic rocks. Instead of envisaging a symmetry decrease by phase transition upon slow cooling (i.e. a retrograde feature)[21], we propose that the tetragonal structure occurs during growth under low-temperature metamorphic conditions (i.e. a prograde feature), as also observed in grossular-rich garnets from contact metasomatic and hydrothermal ore deposits[37]. Microstructural and petrological

210 indications supporting a direct tetragonal growth, rather than an inversion from a cubic precursor, are
211 the presence of sector twinning and the general lack of evidence for now tetragonal garnets having
212 formed at higher *P*–*T* metamorphic conditions, from which they would have cooled /decompressed.
213 The Cazadero sample is particularly useful in constraining this low-*T* monometamorphic
214 process, as the garnet preserves concentric and oscillatory growth zoning, and contains abundant
215 inclusions of very low-*T* minerals, such as stilpnomelane and deerite (Fig. 2a, 5), which are absent
216 from the rock matrix. In addition, the sectored distribution of inclusions in garnet from Pfitscher Joch,
217 which coincide with the optical sectors in the grain itself (Fig. 2c; Supplementary Figure 1;
218 Supplementary Videos S3 and S4 online), provides robust evidence that sector twinning is a growth
219 feature[38]. The possibility that the tetragonal structure formed after any hypothetical lower symmetry
220 precursor is not supported by our data. Instead, the occurrence of orthorhombic, monoclinic and even
221 triclinic symmetries has been so far only been reported only for 'uncommon' garnet compositions,
222 such as hydrogarnet and ugrandite[14, 15].
223 We argue that preservation of the tetragonal structure is favoured in rocks that were not
224 metamorphosed to higher temperature, where a transition to the cubic form (and a different chemical
225 composition) would occur. The data from the Pfitscher Joch schist, which records the highest
226 metamorphic temperatures of the sample studied (500–550°C) and shows the closest approach to a
227 cubic symmetry (Supplementary Table S2), supports this inference.
228 Concerning the possible *P*–*T* conditions at which the tetragonal–cubic inversion might take
229 place, as observed experimentally in leucite[39] and grossular[37], we have performed annealing
230 experiments on garnet crystals from Cazadero, both in an ambient-pressure furnace at 950 °C for 72
231 hours, and in a piston-cylinder at 1 GPa, 1000°C for 232 hours. In both cases the recovered garnets
232 remained anisotropic. These results suggest that the peculiar composition of the garnets documented
233 in this study is resistant to inversion to a cubic structure, and that significant changes in garnet
234 composition (increase of pyrope and decrease of grossular components) are required for such an
235 inversion.
236 The lowering of symmetry observed here would normally be interpreted as the result of the
237 partitioning of the larger Ca and smaller Fe^{2+}, Mg and Mn cations within non-equivalent *X* sites in the
238 structure as proposed, but not unequivocally demonstrated, in earlier studies[21]. Thermodynamic
239 investigation of the mixing properties along the grossular–almandine binary has suggested the

240 occurrence of an ordered compound with composition $Fe_2CaAl_2(SiO_4)_3$, with a Ca–Fe ratio similar to
241 that measured in the tetragonal garnets studied here[40]. However, the results of our XRD and EDT
242 analyses do not provide evidence for ordering, either short- or long-range, of divalent cations in the
243 garnet structure. Therefore, the cause of the tetragonal symmetry remains an open question that
244 requires further investigation, possibly with the aid of spectroscopic techniques[14].
245 Investigating the possible causes and processes arising from cation partitioning is "challenging
246 but vital"[14] for the major implications of non-ideality on the thermodynamic properties of garnet solid
247 solution[41], on the stability and composition of this mineral during metamorphism, on inter- and
248 intracrystalline diffusional processes and their applications[42], and on the behaviour of synthetic
249 nonsilicate garnet used in technological applications[14]. It follows that the tetragonal nature of crystals
250 grown under low-grade metamorphic conditions requires a reconsideration of the crystal-chemical and
251 thermodynamic properties of garnet. Due to the wide pressure–temperature–composition stability field
252 of garnet, the latter are key for constraining the pressure–temperature–time history of rocks from the
253 shallow crust to deep lithosphere, from which large-scale tectonic processes may be inferred. Using
254 incorrect thermodynamic properties and mixing models for a relevant metamorphic mineral such as
255 garnet affects our ability to model the geodynamic processes attending metamorphism, although the
256 magnitude of such effects awaits further investigation.
257 The possible limitations of thermodynamic parameters pertaining to the onset of garnet growth at low
258 temperature have already been highlighted[43], and could explain why current mixing models in some
259 cases fail to predict the presence of garnet in low-temperature metamorphic rocks[3, 44]. As the lack of
260 stability of one phase could also be due to the use of an inappropriate effective bulk composition, we
261 performed a simple test by analysing the stability and composition of garnet in a model SiO_2–Al_2O_3–
262 FeO–MnO–MgO–CaO–H_2O system, coinciding with a typical tetragonal garnet composition measured
263 in this work at Cazadero ($Alm_{62}Grs_{25}Sps_{10}Pyp_3$, see Supplementary Table S1), assuming the
264 presence of a pure H_2O volatile phase that permits the inclusion of hydrous phases. The results of
265 phase equilibria modelling in the range 250–850 °C and 0.2-1.5 GPa, performed with the Perple_X
266 software[45]and using the most recent thermodynamic dataset and solution models[46], are reported in
267 Fig. 8. The calculations show that the target (input) garnet composition is stable within an uncertainty
268 of ± 1 mol% at T > 500 °C, and that temperature has to be almost 650°C to match exactly the input
269 composition. In this respect, the predicted concentration of the spessartine component shows the

poorest match for that in the natural garnet composition. The results of the modelling do not differ significantly when a mixed H_2O–CO_2 fluid is present to account for low a_{H2O} conditions. The predicted temperature conditions of garnet stability (>500 °C) contrast with the much lower temperatures (<350 °C) proposed in the literature[23] that are supported an inclusion assemblage including deerite, chlorite and stilpnomelane. This test reinforces the perspective that existing thermodynamic properties of garnet that grows in the initial stages of subduction and in the lowest-grade part of orogenic belts need to be re-assessed. The characterization of natural samples with a tetragonal structure, such as in this study, may be used to refine the calorimetric properties and mixing parameters of garnet at low temperature.

Acknowledgements

B.C. acknowledges financial support from University of Padova (grant BIRD183984) and MIUR (grant 2017ZE49E7). We thank Bob Coleman for discussion about the geology of the Cazadero sample, Sarah Penniston-Dorland for kindly providing the Jenner sample, Matteo Alvaro for help with XRD analyses, and Stefano Poli for highlighting the importance of calcium in metamorphic rocks.

Author Contributions

B.C. developed the concept, collected the samples and carried out the petrographic and microstructural study. O.B. and L.P. did the SEM and EMP characterization of samples; T.E. and L.P. did the EBSD characterization; G.D.V. did the FTIR analyses; E.M. and C.V. performed the HRTEM and EDT studies; F.N. did the XRD characterization; B.C. and T.J. wrote the paper. All authors were involved in multiple revisions of text and figures.

Competing Interests statement

The authors declare no competing financial and non-financial interests.

Data Availability

The datasets generated during and/or analysed during the current study, whether not included in this published article and its Supplementary Information files, are available from the corresponding author on reasonable request.

Methods

Materials

Polished regular (30 μm thick) thin sections and doubly polished 100 to 200 μm thick sections were obtained from the six studied samples of blueschists, phyllite and schist.

In addition, single crystals of garnet were handpicked after selective High Voltage Pulse Fragmentation using Selfrag AG Lab system. 200 μm thick doubly-polished equatorial wafers of single crystals were then prepared for optical observation.

Electron Microprobe Analysis (EMPA)

The major element composition of garnet and the X-ray elemental maps were obtained with a Jeol JXA 8200 Superprobe at the Dipartimento di Scienze della Terra, Università di Milano, Italy. Analytical parameters were 15 kV accelerating voltage, 5 nA current, counting time of 30 s on peak and 10 s on background.

Fourier-Transform Infrared Spectroscopy (FTIR)

Single crystals from Cazadero blueschist and from Pfitscher Joch and eastern Alps phyllites were manually separated from the rocks and doubly polished such as to obtain an equatorial slice through the garnet, with thickness ranging between 325 and 315 μm. FTIR raster maps[47] were acquired with aperture 40 × 40 μm^2 using a Bruker Hyperion 3000 microscope equipped with a KBr broadband beam splitter, a 15X objective and a liquid nitrogen-cooled MCT detector at Istituto Nazionale di Fisica Nucleare (LNF- INFN), Frascati, Italy. A conventional (Globar) source was used for the IR beam; the nominal resolution was set at 4 cm^{-1} and 128 scans were averaged for both spectrum and background. High-resolution FTIR images were collected with a 64 × 64 pixel focal-plane array (FPA) of liquid nitrogen-cooled MCT detectors, coupled to a 15X Schwarzschild objective. The nominal resolution was set at 8 cm^{-1} and 64 scans were averaged for each spectrum and background; in these conditions each image covers an area of 170 × 170 μm, with a spatial resolution of ~5 μm [38,48]. The final images were obtained as a mosaic of several single images, displacing the sample along a grid at 170 μm step, such as to cover the desired area.

330 Electron Backscattered Diffraction (EBSD)

331 Thin sections of samples from Cazadero and Farinole were prepared with a mechanical polish using 1
332 μm diamond paste. After garnet grains were identified and imaged optically the section was given a
333 final chemical-mechanical polish using 50 nm colloidal silica dispersion in NaOH. After polishing,
334 garnets were imaged using backscattered electron (BSE) atomic contrast imaging with a Tescan
335 Mira3 field emission gun scanning electron microscope (FEG-SEM). Two garnet grains were then
336 mapped by electron backscatter diffraction (EBSD). Electron backscatter patterns (EBSPs) were
337 collected from the garnets and the surrounding matrix in orthogonal grids using a Nordsly Nano high
338 resolution detector and Oxford Instruments Aztec 2.4 acquisition software package on the Mira3 FEG-
339 SEM. EBSD analyses were collected with a 20 kV accelerating voltage, 70° sample tilt, ~20 mm
340 working distance, and 18 nA beam current. EBSPs were collected with the following parameters; an
341 acquisition speed of ~40 Hz, 64 frames were collected for a background noise subtraction, 4 x 4
342 binning, high gain, a Hough resolution of 60, and band detection min/max of 6/8. Maps were collected
343 in orthogonal grids with a step size between 2.0 μm and 2.5 μm. Mean angular deviation values of the
344 electron backscatter patterns for the maps ranged between 0.36 and 0.35. Individual garnet grains
345 were indexed using the Grossular match unit based on the unit cell parameters of 1 with a = b = c =
346 11.8451 Å. Glaucophane of the surrounding matrix was indexed using the match unit Glaucophane
347 after the unit cell parameters of 2. Additional matrix and inclusion minerals are apatite and quartz.
348 Apatite was indexed using the oxyapatite match unit from the cell parameters of 3, and quartz was
349 indexed using the Quartz new match unit based on the unit cell parameters of 4.
350 Post-processing the EBSD data was undertaken with Oxford Instruments Channel 5.11 software suite.
351 All EBSD data was given a wild-spike noise reduction and a seven nearest neighbour zero-solution
352 correction, no other corrections were applied. Using Tango suite of Channel 5 the following EBSD
353 maps were produced:
354 1) Colored phase maps, garnet is blue, glaucophane is green, quartz is red, and apatite is yellow;
355 2) All Euler crystallographic orientation map;
356 3) Texture component maps (0 – 2.5°), colored with a rainbow scheme revel misorientation from the
357 mean orientation of the grain as determined using the grain detect function of Tango. Blue domains
358 are close to the average orientation, while warm colors represent higher degrees of misorientation

359 from the grain average. Apparent misorientation from the grain average is due to changes in the unit
360 cell parameters related to intragranular chemical variation.
361 4) Grain misorientation map, using the grain rotation orientation direction (GROD)-hyper function of
362 Channel5, which helps visualize the substructure of the grains by plotting the deviation angle of each
363 pixel and the disorientation axis from the mean grain orientation, grain boundaries are defined as
364 >10°.
365 Simultaneous with EBSD mapping, energy dispersive X-ray spectra were collected from each pixel.
366 The X-ray spectra for the maps were collected using an Oxford instruments X-Max detector and were
367 processed using the Aztec 2.4 software package.
368
369 High-Resolution Transmission Electron Microscopy (HRTEM)
370 TEM investigations were performed by a JEOL 2010 microscope, working at 200 kV, with ultra-high
371 resolution (UHR) pole piece and point-to-point resolution of 0.19 nm. The microscope is equipped with
372 semi-STEM control and ultra-thin window energy dispersive spectrometer (EDS ISIS Oxford). Data
373 were recorded by an Olympus Tengra CCD camera (2k x 2k x 14 bit). Sample preparation has been
374 done by Ar+ ion milling (Dual Ion Mill Gatan and PIPS Gatan 691). TEM grids were extracted from
375 polished petrographic sections, selecting at least two birefringent garnets for each sample (AUS,
376 FRAN and SPIA). Ion milling had two main consequences: on one side, the obtainment of ultrathin
377 samples (less than 100 nm) significantly reduced the garnet birefringence colour in the petrographic
378 microscope, providing almost extinct crystals; on the other side, many crystallographic features,
379 observed in the 30 μm thick samples, were no longer visible, thus complicating the identification of
380 features such as sector boundaries, possible twinning planes or mottled pattern.
381
382 Electron diffraction tomography (EDT)
383 EDT data collections[49,50,51] were performed by a Zeiss Libra TEM operating at 120 kV and equipped
384 with a LaB_6 source and a Bruker EDS detector XFlash6T-60. EDT acquisitions were done in STEM
385 mode after defocusing the beam. A beam size of about 150 nm in diameter was obtained by inserting
386 a 5 μm C2 condenser aperture. EDT data were recorded by a background-free single-electron ASI
387 Timepix detector[52], which allows an extremely mild illumination thus preventing any alteration or
388 amorphization of the sample.

EDT data sets were acquired with and without precessing the beam. Precession was obtained by a Nanomegas Digistar P1000 device, with a semi-angle of about 1°. EDT data used for dynamical structure refinement were acquired with precessing beam for better reflection intensity integration, in tilt steps of 1° for a total tilt range of -60°/+60°. A camera length of 180 mm was used, equivalent to a resolution of about 0.75 Å. Data analysis, including cell parameter determination, reflection intensity integration, ab-initio structure determination and dynamical refinement[53], was performed by the PETS-JANA package.

EDT intensity distribution suggest again a tetragonal symmetry. Moreover, clear violations on extinction conditions are observed in the reconstructed 3D diffraction volume, consistent with space group $I4_1/a$ (Fig. 6a, Supplementary Fig. S4 online). Ab-initio structure solution was achieved in space groups *I*a-3*d*, $I4_1/acd$ and I41/a. Residuals obtained by dynamical refinement in these space groups are comparable, with differences of only 1% in R1. The two larger crystallographic sites occupied by Fe and Ca appear quite similar, both in terms of Fe/Ca-O interatomic distances and in terms of geometry. A tentative refinement of the distribution of Ca and Fe resulted in a comparable partial occupancy for the two sites.

Single-Crystal X-Ray Diffraction (XRD)

A birefringent garnet from Jenner was investigated by single-crystal X-ray diffraction using two different X-ray diffractomers. Using a point detector diffractometer controlled by the software SINGLE software[54], which is designed to apply the 8-centering positions, allowed to measure the unit-cell parameters with very high accuracy and precision. We collected 45 different reflections (each measured in 8 different positions) and the results (Supplementary Tab. S2 online) clearly indicate a tetragonal symmetry with a = b = 11.6064(4) Å, c = 11.6146(8) Å, volume = 1564.59(13) Å3. The difference between a,b and c axes is well above 10 times the experimental uncertainty and thus the tetragonal cell is definitively reliable. The c/a ratio = 0.0007, is in agreement with the value of 0.0009 recently determined for a hydrous natural tetragonal garnet.

The same crystal was then studied using a second single-crystal diffractometer to collect complete intensity data and obtain structural data. We have measured a spherical shaped crystal with an average radius of 0.08 mm up to $2\theta = 82°$ and collected the full Ewald sphere summing a total of 47660 reflections of which 1279 unique (Rint = 0.045). WINGX package and SHELX software[17,55,56]

were used for structure refinement. The systematic absences and the statistical analysis of the intensities are consistent with $I4_1/acd$ space group and the structure (see Supplementary Tab. 2 online) was refined starting from recently published structural models[57,58,59]. Our model does not report the F11 and O22 sites (see[17]) because the investigated garnet is anhydrous and does not contain any F. However, our structure refinement shows an excellent agreement factor with R1 = 0.021 to indicate that the space group here adopted is absolutely reliable. This agreement factor is better, or at least comparable, with those obtained for previous refinements on natural hydrous tetragonal garnets which show the same $I4_1/acd$ space group as in our work. In terms of site occupancy, Fe, Ca, Mn and Mg occupy the X1 and X2 crystallographic sites and we do not observe any site preferences among such elements within these sites. This is definitively confirmed by the X1-O an X2-O average bond distances, which are practically identical within one uncertainty (e.g. Ca, for example, has a much longer cation radius with respect to the other ions and this would be strongly evident on the bond distances in case of Ca preference for one of the two sites). All crystallographic information are deposited with the CIF file (Supplementary Data S1 online).

435 **Figure Captions**
436
437 **Figure 1** Macroscopic views and petrographic features of the studied blueschists, with emphasis on
438 optical anisotropy of garnets. a: Jenner; b: Cazadero; c: Farinole.
439
440 **Figure 2** Typical examples of birefringence in the studied garnets. **a**. 200-μm-thick wafer of an isolated
441 euhedral crystal from Cazadero, California, with sector zoning defined by three pairs of opposite
442 sectors. Arrows point to inclusions of riebeckite. Crossed polarizers (XP) and lambda plate (λ). **b**.
443 Regular 30-μm thin section view of a partly resorbed garnet set in a fine-grained matrix of Na-
444 amphibole. Arrows point to the subtle concentric oscillatory zoning. Cazadero, XP. **c**. Optically sector-
445 zoned garnet porphyroblast in a biotite-graphite schist from Pfitscher Joch. 100-μm-thick section, XP.
446 **d**. Optically sector-zoned garnet in a chlorite-muscovite phyllite from the eastern Alps. 100-μm-thick
447 section, XP, λ. **e**: 30-μm thin section view of a sector-zoned garnet in a blueschist from Farinole,
448 Corsica. Arrows indicate the boundaries between sectors. White square indicates area enlarged in (e).
449 XP, λ. **f**. Detail of (e) showing the mottled pattern of birefringence within sectors. Arrow indicates the
450 sharp line, that is not a microfracture, corresponding to the sector boundary. XP. The B-B' line
451 corresponds to the EMP transect reported in Fig. 3c. **g**. Detail of a garnet in a blueschist from Jenner,
452 California showing a well-developed mottled pattern. Arrows indicate a poorly defined sector
453 boundary. XP, λ.
454
455 **Figure 3** Compositional patterns and inhomogeneities in the studied garnets. **a**. Series of images
456 showing, from left to right, optical and BSEM view of a sector-zoned garnet from Cazadero, followed
457 by the X-ray maps with the distribution of Mn, Ca and Fe. White arrows point to Ca-high, Fe-low
458 layers, black arrows to Ca-low, Fe high layers in the oscillatory-zoned part of the crystal. The A-A' line
459 corresponds to the EMP transect reported in Fig. 3c. **b**. Details of a zone with marked mottled
460 birefringence in a garnet from Jenner. From left to right optical and BSEM views, Ca and Fe X-ray
461 maps of the same area. Arrows like in (a). The C-C' line corresponds to the EMP transect reported in
462 Fig. 3c. **c**. Major element compositional features in crystals of blueschists along transects in Fig. 1f, 3a
463 and 3b. A-A': Cazadero: transect from rim (A) to core (A') of crystal. The features related to oscillatory
464 zoning are apparent on the left part of profile. B-B': Farinole and C-C': Jenner. Details of the bands

and patches of Ca-Fe variations. Peaks and troughs have maximum widths of 10-20 μm. For all transects the vertical arrows locate the counterbalancing variations of Ca and Fe mirroring each other.

Figure 4 Triangular compositional plot of all EMP garnet analyses. Dashed ellipse marks the compositions of the outermost rims of Pfitscher Joch micaschist and of Maniva Pass phyllite, characterized by lower Ca and higher Mg contents.

Figure 5 FTIR imaging and the distribution of the hydrous components in a garnet from Cazadero. **a**. Optical image of the examined sample. **b**. Distribution of the hydrous components resulting from a grid of 40x40 μm^2 single spots. **c**. High-resolution image collected as a grid (reported on the image) of 12 FPA spots, each covering 170x170 μm^2; the image clearly shows that the hydrous components are strictly related to the included fibrous minerals, while the garnet host is anhydrous. Both images were obtained by integrating the signal in the OH-stretching 3700-3400 cm^{-1} range. The intensity of the absorption is proportional to the colour scale on the left, where blue = zero and red = maximum. **d**. Selected single spectra (plotted with the same absorbance scale), collected with a 40x40 μm beam in a fibrous-rich area toward the crystal core (red line), and in a clean area in the garnet host (black line). The spectrum collected in the garnet host is totally flat, indicating the sample to be totally anhydrous; the spectrum collected in the hydrous zone shows a convoluted absorption (see Methods); the peaks of amphibole (Amp) and phyllosilicate (Chl, a phase close in composition to a chlorite) are evidenced. Spectra collected in the NIR (6000-4000 cm^{-1}) range in the hydrated core (not shown) display only a weak band at 4170 cm^{-1} while no absorption occurs at wavenumbers > 5000 cm^{-1}; this indicates the presence of OH-groups only as hydrous component in the sample.

Figure 6 Structural TEM features of garnets from Cazadero. **a**. Section of the 3D diffraction volume obtained by EDT data. (a) 0kl plane, showing reflections 0kl: k,l ≠ 2n, not consistent with a Ia-3d and I41/acd symmetry, marked by red arrows. **b**. HRTEM: HR imaging of a garnet from Cazadero (corresponding [111] SAED pattern in the inset). The planar discontinuity is consistent with the occurrence of a twinning plane. Dark contrast around the twinning plane is due to local crystal structural strain.

Figure 7 Petrographic and electron microscopic images of an anisotropic garnet from Cazadero. **a.** Crossed-polarized optical photomicrograph of garnet showing well-developed sector zoning. **b.** Phase recognition map from same field of view as (a) indexed with electron backscatter diffraction. Red = tetragonal garnet; blue = glaucophane; green = quartz. **c.** Texture component map (0 – 2.5°) with a rainbow color scheme revels misorientation from the mean crystallographic orientation of the grain. Blue-green domains are close to the average orientation, while warm colors represent higher degrees of misorientation from the grain average. Apart from misorientation related to a fracture on top left, apparent misorientation from the grain average is an artefact due to changes in the unit cell parameters related to intracrystalline chemical variation.

Figure 8 Thermodynamic calculation of the stability and composition of garnet. The model used coincides with an $Alm_{62}Grs_{25}Sps_{10}Pyp_3$ garnet composition in the SiO_2–Al_2O_3–FeO–MnO–MgO–CaO–H_2O system and assumes the presence of a saturating pure H_2O volatile phase. Background color ranges from dark blue (low concentrations) to red (high concentrations). Thin red lines are isopleths, labelled in mol%, of the garnet components considered in each panel (from top left counterclockwise pyrope, almandine, grossular and spessartine). Thick black lines are isopleths of the target (input) composition, reported within black labels. Thin black lines are isopleths of composition corresponding to ± 1 mol% of the input composition. Central inset reports the P-T location of the target isopleths.

514 **References**

1 Baxter, E. F., Caddick, M. J. & Ague, J. J. Garnet: Common Mineral, Uncommonly Useful. *Elements* **9**, 415-419 (2013).

2 Spear, F. S., Selverstone, J., Hickmott, D., Crowley, P. & Hodges, K. V. P-T paths from garnet zoning: A new technique for deciphering tectonic processes in crystalline terranes. *Geology* **12**, 87-90 (1984).

3 Caddick, M. J. & Kohn, M. J. Garnet: Witness to the Evolution of Destructive Plate Boundaries. *Elements* **9**, 427-432 (2013).

4 Stagno, V., Ojwang, D. O., McCammon, C. A. & Frost, D. J. The oxidation state of the mantle and the extraction of carbon from Earth's interior. *Nature* **493**, 84-88 (2013).

5 Spear, F. S. & Kohn, M. J. Trace element zoning in garnet as a monitor of crustal melting. *Geology* **24**, 1099-1102 (1996).

6 Page, F. Z., Essene, E. J., Mukasa, S. B. & Valley J. W. A Garnet–Zircon Oxygen Isotope Record of Subduction and Exhumation Fluids from the Franciscan Complex, California. *J. Petrol.* **55**, 103-131 (2013).

7 Dragovic, B., Gatewood, M. P., Baxter, E. F. & Stowell H. H. Fluid production rate during the regional metamorphism of a pelitic schist. *Contrib. Mineral. Petrol.* **173**, (2018).

8 Pollington, A. D., & Baxter, E. F. High resolution Sm–Nd garnet geochronology reveals the uneven pace of tectonometamorphic processes. *Earth Planet. Sci. Lett.* **293**, 63-71 (2010).

9 Baxter, E. F., & Scherer, E. E. Garnet geochronology: timekeeper of tectonometamorphic processes. *Elements* **9**, 433-438 (2013).

10 Van Mierlo, W., Langenhorst, F., Frost, D. & Rubie, D. Stagnation of subducting slabs in the transition zone due to slow diffusion in majoritic garnet. *Nature Geosci.* **6**, 400 (2013).

11 Rubatto, D. & Hermann, J. Experimental zircon/melt and zircon/garnet trace element partitioning and implications for the geochronology of crustal rocks. *Chem. Geol.* **241**, 38-61 (2007).

12 Pertermann, M., Hirschmann, M. M., Hametner, K., Günther, D. & Schmidt, M. W. Experimental determination of trace element partitioning between garnet and silica‐rich liquid during anhydrous partial melting of MORB-like eclogite. *Geochem. Geophys. Geosy.* **5**, (2004).

13 Viete, D.R. *et al.* Metamorphic records of multiple seismic cycles during subduction. *Science Advances* **4**, eaaq0234 (2018).

14 Geiger, C.A. Garnet: A key phase in nature, the laboratory, and technology. *Elements* **9**, 447-452 (2013).

15 Grew, E.S. *et al.* Nomenclature of the garnet supergroup. *Amer. Miner.* **98**, 785-810 (2013).

16 Suggate, S.M. & Hall, R. Using detrital garnet compositions to determine provenance: a new compositional database and procedure. *Geol. Soc. London Sp. Pub.* **386**, 373-393 (2014).

17 Antao, S.M. & Cruikshank, L.A. Crystal structure refinements of tetragonal (OH, F)-rich spessartine and henritermierite garnets. *Acta Cryst. B* **74**, 104-114 (2018).

18 Andrut, M., Wildner, M. & Beran, A. The crystal chemistry of birefringent natural uvarovites. Part IV. OH defect incorporation mechanisms in non-cubic garnets derived from polarized IR spectroscopy. *Eur. J. Mineral*. **14**, 1019-1026, (2002).

19 Antao, S.M. The mystery of birefringent garnet: is the symmetry lower than cubic? *Powder Diffraction* **28**, 265-272 (2013).

20 Hofmeister, A. M., Schaal, R. B., Campbell, K. R., Berry, S. L. & Fagan, T. J. Prevalence and origin of birefringence in 48 garnets from the pyrope-almandine-grossularite-spessartine quaternary. *Amer. Miner.* **83**, 1293-1301 (1998).

21 Griffen, D.T., Hatch, D.M., Phillips, W.R. & Kulaksiz, S. Crystal chemistry and symmetry of a birefringent tetragonal pyralspite$_{75}$-grandite$_{25}$ garnet. *Amer. Miner.* **77**, 399-406 (1992).

22 Coleman, R.G. & Lee, D.E. Glaucophane-bearing metamorphic rock types of the Cazadero area, California. *J. Petrol.* **4**, 260-301 (1963).

23 Ukar, E. & Cloos, M. Low-temperature blueschist-facies mafic blocks in the Franciscan mélange, San Simeon, California: Field relations, petrology, and counterclockwise P-T paths. *GSA Bulletin* **126**; 831–856 (2014).

24 Tsujimori, T., Matsumoto, K., Wakabayashi, J. & Liou, J.G. Franciscan eclogite revisited: Reevaluation of the P–T evolution of tectonic blocks from Tiburon Peninsula, California, USA. *Mineral. Petrol.* **88**, 243–267 (2006).

25 Oh, C-W. & Liou, J.G. Metamorphic evolution of two different eclogites in the Franciscan Complex, California, USA. *Lithos* **25**, 41-53 (1990).

26 Krogh, E.J., Oh, C.W. & Liou, J.G. Polyphase and anticlockwise P-T evolution for Franciscan eclogites and blueschists from Jenner, California, USA. *J. Metamorph. Geol.* **12**, 121-134 (1994).

27 Lahondere, D. Le métamorphisme éclogitique dans les orthogneiss et les métabasites ophiolitiques de la région de Farinole (Corse). *Bull Soc géol France* **4**, 579-585 (1988).

28 Selverstone, J. & Munoz, J.L. Fluid heterogeneities and hornblende stability in interlayered graphitic and nongraphitic schists (Tauern Window, Eastern Alps). *Contrib. Mineral. Petrol.* **96**, 426-440 (1987).

29 Shtukenberg, A. & Punin, Y.O. *Optically Anomalous Crystals*. Springer, 279 pp. (2007).

30 Lee, D. E., Coleman, R.G. & Erd, R.C. Garnet types from the Cazadero area, California. *J. Petrol.* **4**, 460-492 (1963).

31 Rice, A.H.N. *et al.* Textural sector-zoning in garnet: Theoretical patterns and natural examples from Alpine metamorphic rocks. *Austrian J. Earth Sci.***99**, 70-89 (2006).

32 Yardley, B.W.D., Barber, J.P. & Gray, J.R. (1987) The metamorphism of the Dalradian rocks of western Ireland and its relation to tectonic setting. *Phil. Trans. R. Soc. London* **321**, 243-270 (1987).

33 Franceschelli, M., Memmi, I. & Ricci, C.A. Ca distribution between almandine-rich garnet and plagioclase in pelitic and psammitic schists from the metamorphic basement of north-eastern Sardinia. *Contrib. Mineral. Petrol.* **80**, 285-295 (1978).

34 Brown, D. & Mason, R.A. An occurrence of sectored birefringence in almandine garnet. *Can. Mineral.* **32**, 105-110 (1994).

35 Weller, O.M., Wallis, S.R., Aoya, M. & Nagay, T. Phase equilibria modelling of blueschist and eclogite from the Sanbagawa metamorphic belt of southwest Japan reveals along‐strike consistency in tectonothermal architecture. *J. Metamorph. Geol.* **33**, 579–596 (2015).

36 Davis, P. B. & Whitney, D. L. Petrogenesis of lawsonite and epidote eclogite and blueschist, Sivrihisar Massif, Turkey. *J. Metamorph. Geol.* **24**, 823–849 (2006).

37 Allen, F. M. & Buseck, P. R. XRD, FTIR, and TEM studies of optically anisotropic grossular garnets. 1988 *Amer. Miner.* **73**, 568-584 (1988).

38 Jamtveit, B. & Andersen, T. B. Morphological instabilities during rapid growth of metamorphic garnets. Phys. Chem. Minerals. **19**, 176–184 (1992).

39 Lange, R. A., Carmichael, I. S. E. & Stebbins, J. F. Phase transitions in leucite ($KAlSi_2O_6$), orthorhombic $KAlSiO_4$, and their iron analogues ($KFeSi_2O_6$, $KFeSiO_4$). *Amer. Miner.* **71**, 937-945 (1986).

40 Cressey, G., Schmid, R. & Wood, B.J. Thermodynamic properties of almandine-grossular garnet solid solutions. *Contrib. Mineral. Petrol.* **67**, 397-404 (1978).

41 Ganguly, J., Cheng, W. & Tirone, M. Thermodynamics of aluminosilicate garnet solid solution: new experimental data, an optimized model, and thermometric applications. *Contrib. Mineral. Petrol.* **126**, 137-151 (1996).

42 Ganguly, J. Cation Diffusion Kinetics in Aluminosilicate Garnets and Geological Applications. in *Diffusion in Minerals and Melts* (eds. Zhang, Y. & Cherniak, D. J.) 559-601 (MSA RIMG, 2010).

43 Dragovic et al Pulsed dehydration and garnet growth during subduction revealed by zoned garnet geochronology and thermodynamic modeling, Sifnos,Greece EPSL **413**, 111-122 (2015).

44 Palin, R.M. & White, R.W. Emergence of blueschists on Earth linked to secular changes in oceanic crust composition. *Nature Geoscience* **9**, 60-64 (2016).

45 Connolly, J.A.D. The geodynamic equation of state: what and how. *Geochem. Geophys. Geosy.* **10**, Q10014. (2009)

46 White, R.W., Powell, R. and Johnson, T.E. The effect of Mn on mineral stability in metapelites revisited: New a–x relations for manganese-bearing minerals. *J. Metamorph. Geol.* ***32***, 809–828 (2014).

47 Della Ventura, G., Marcelli, A. & Bellatreccia, F. SR-FTIR Microscopy and FTIR Imaging in the Earth Sciences. *RIMG* **78**, 447-479 (2014)

48 Della Ventura, G. *et al.* (2010) Application of micro-FTIR imaging in the Earth sciences. *Analyt. Bioanalyt. Chem.* **397**, 2039-2049 (2010)

49 Kolb, U., Gorelik, T., Kübel, C., Otten, M.T. & Hubert, D. Towards automated diffraction tomography: Part I—Data acquisition. *Ultramicroscopy,* **107**, 507–513 (2007).

50 Mugnaioli, E. & Gemmi, M. Single-crystal analysis of nanodomains by electron diffraction tomography: mineralogy at the order-disorder borderline. *Z. Kristallogr.* **233**, 163–178 (2018).

51 Mugnaioli, E., Gorelik, T. & Kolb, U. “Ab initio” structure solution from electron diffraction data obtained by a combination of automated diffraction tomography and precession technique. *Ultramicroscopy* **109**, 758–765 (2009).

52 Nederlof, I., van Genderen, E., Li, Y.-W. & Abrahams, J.P. *A Medipix quantum area detector allows rotation electron diffraction data collection from submicrometre three-dimensional protein crystals. Acta Cryst. D*, **69**, 1223–1230 (2013).

53 Palatinus, L. *et al.* Structure refinement using precession electron diffraction tomography and dynamical diffraction: tests on experimental data. *Acta Cryst. B*, **71**, 740–751 (2015).

54 Angel, R.J. & Finger, L.W. SINGLE: a program to control single-crystal diffractometers. *J. Appl. Cryst.* **44**, 247-251 (2011).

55 Farrugia, L.J. WinGX and ORTEP for Windows: an update. *J. Appl. Cryst.* **45**, 849-854 (2012).

56 Sheldrick, G.M. Crystal structure refinement with SHELXL. *Acta Cryst. A* **64**, 112–122 (2008).

57 Armbruster, T. *et al.* Structure, compressibility, hydrogen bonding, and dehydration of the tetragonal Mn^{3+} hydrogarnet, henritermierite. *Amer. Miner.* **86**, 147-158 (2001).

58 Boiocchi, M., Bellatreccia, F., Della Ventura, G. & Oberti, R. On the symmetry and atomic ordering in (OH,F)-rich spessartine: towards a new hydrogarnet end-member. *Z. Kristallogr.* **227**, 385–395 (2012).

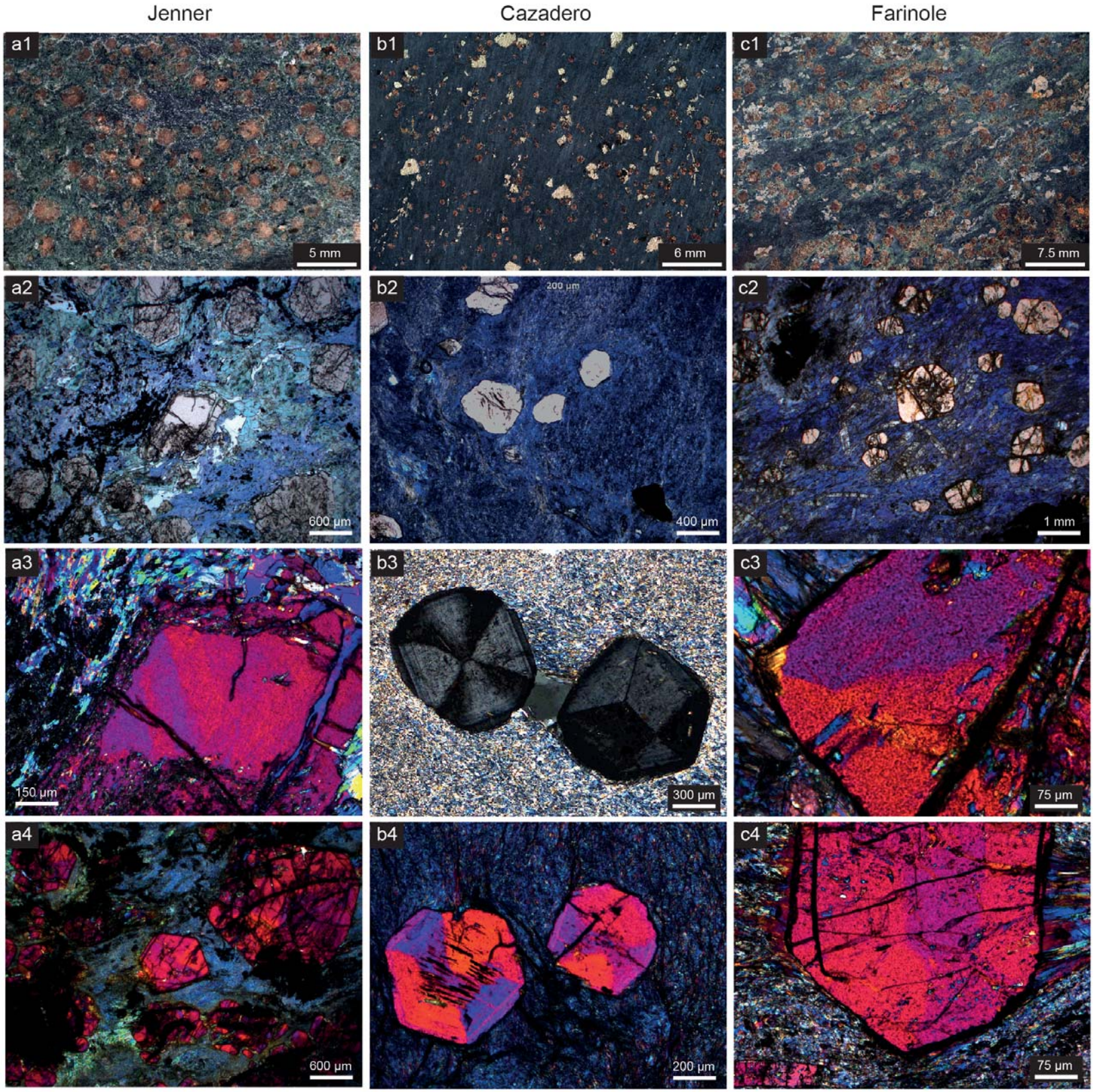
Jenner
Cazadero
Farinole
a1
5 mm
b1
6 mm
c1
7.5 mm
a2
600 µm
b2
200 µm
400 µm
c2
1 mm
a3
150 µm
b3
300 µm
c3
75 µm
a4
600 µm
b4
200 µm
c4
75 µm

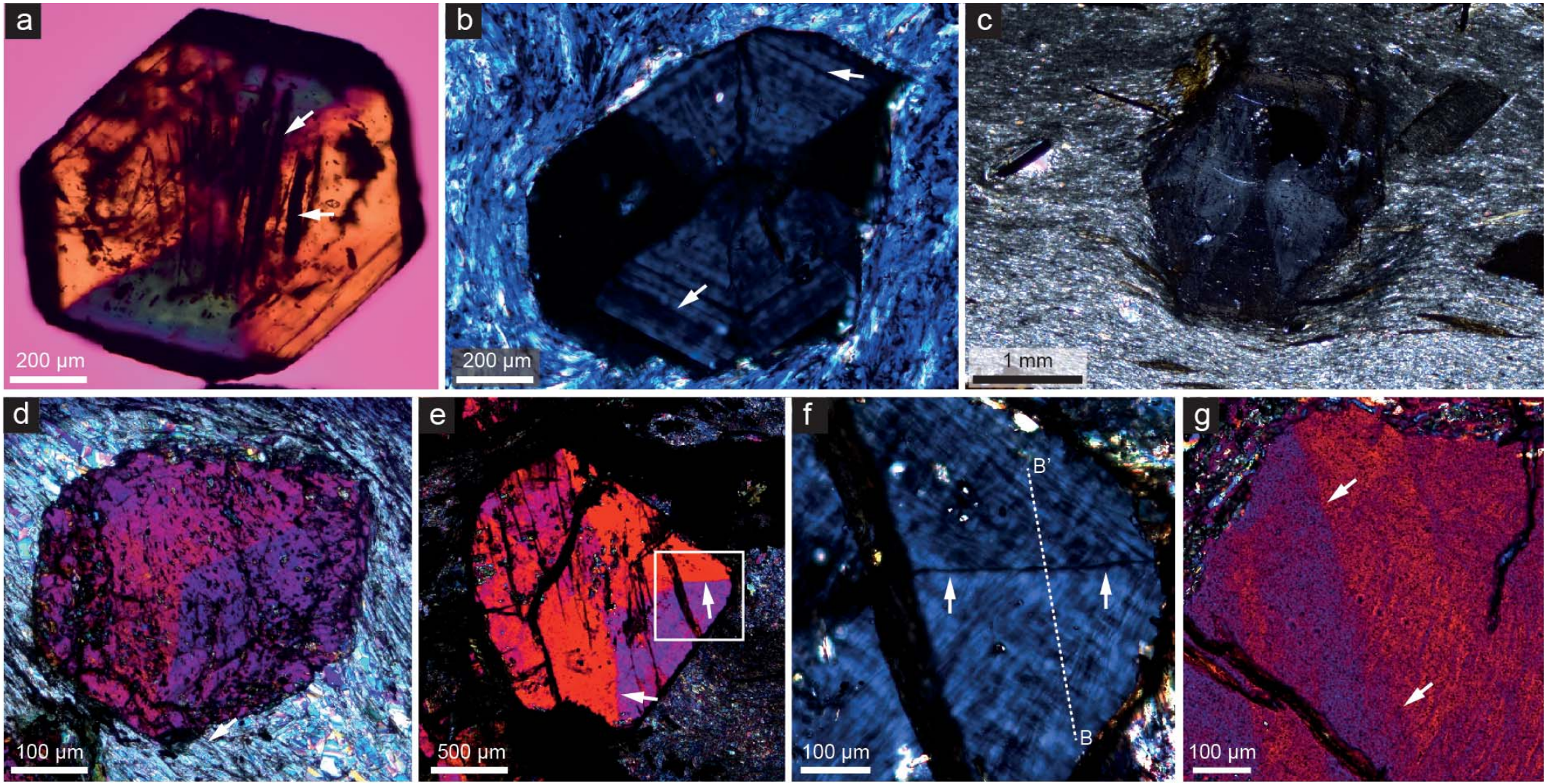
a
200 µm
b
200 µm
c
1 mm
d
100 µm
e
500 µm
f
B'
B
100 µm
g
100 µm

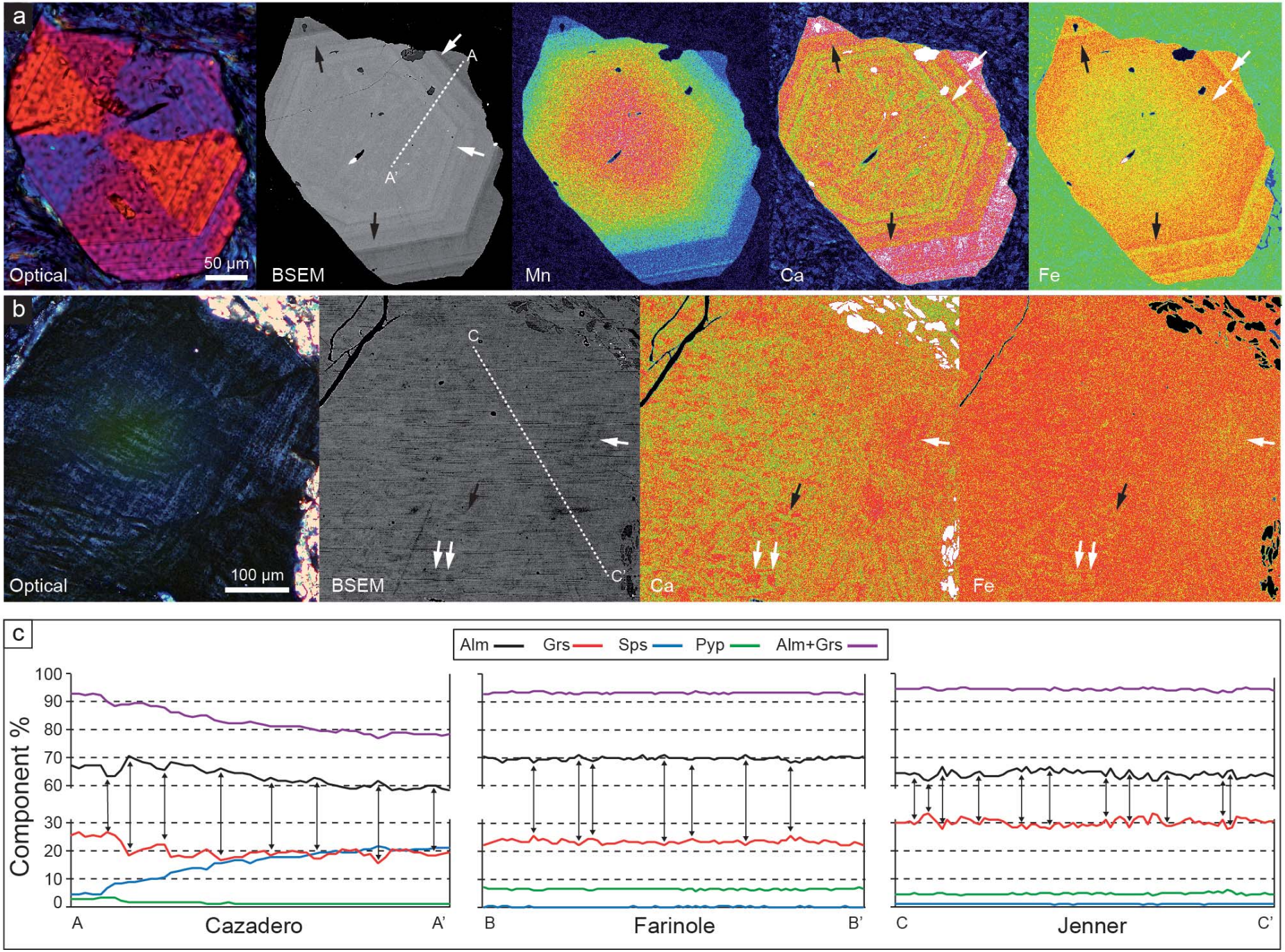
a
Optical
50 µm
BSEM
A
A'
Mn
Ca
Fe
b
Optical
100 µm
BSEM
C
C'
Ca
Fe
c
Alm
Grs
Sps
Pyp
Alm+Grs
Component %
100
90
80
70
60
30
20
10
0
A
Cazadero
A'
B
Farinole
B'
C
Jenner
C'

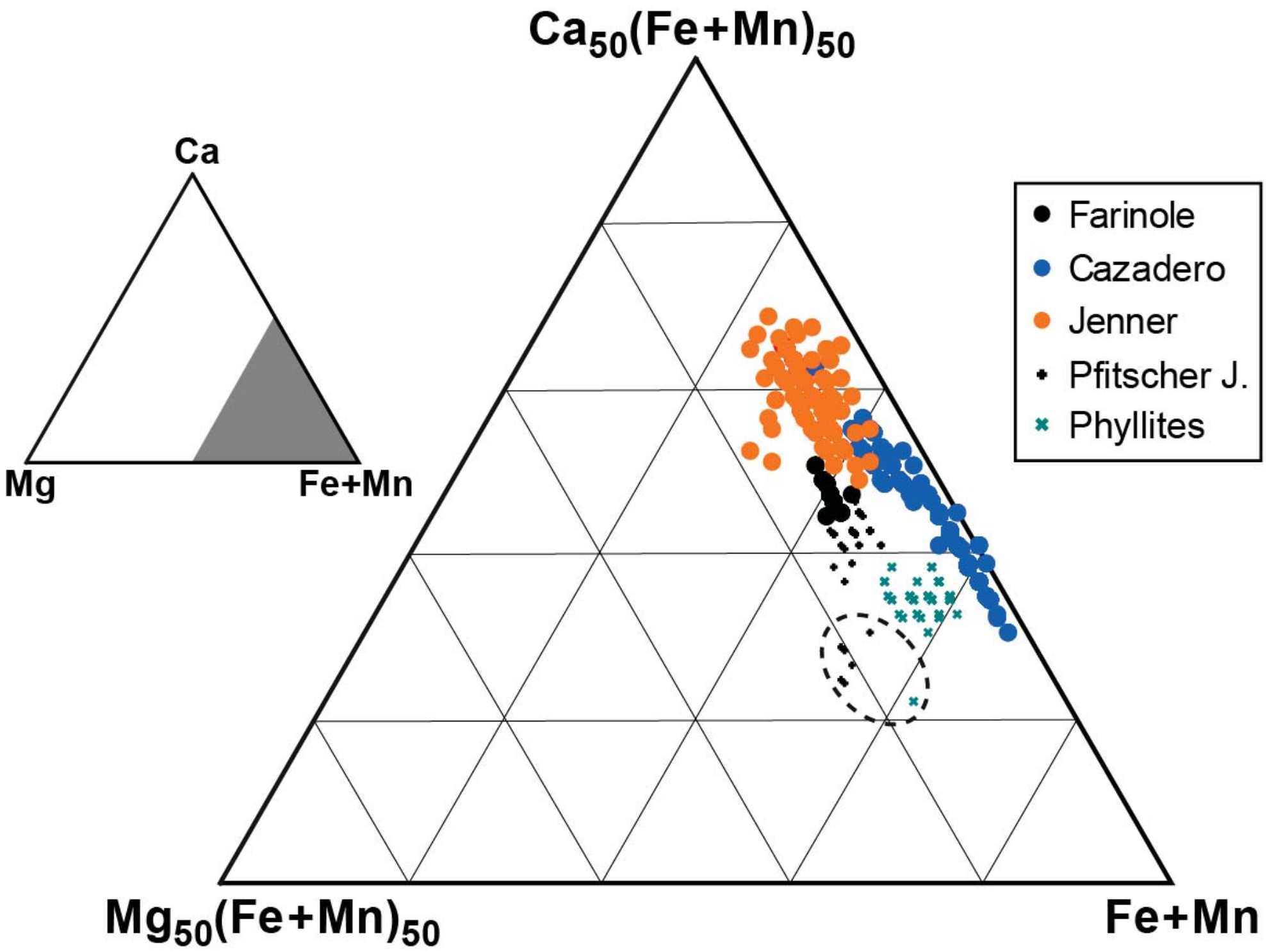
Ca50(Fe+Mn)50
Ca
Mg
Fe+Mn
Farinole
Cazadero
Jenner
Pfitscher J.
Phyllites
Mg50(Fe+Mn)50
Fe+Mn

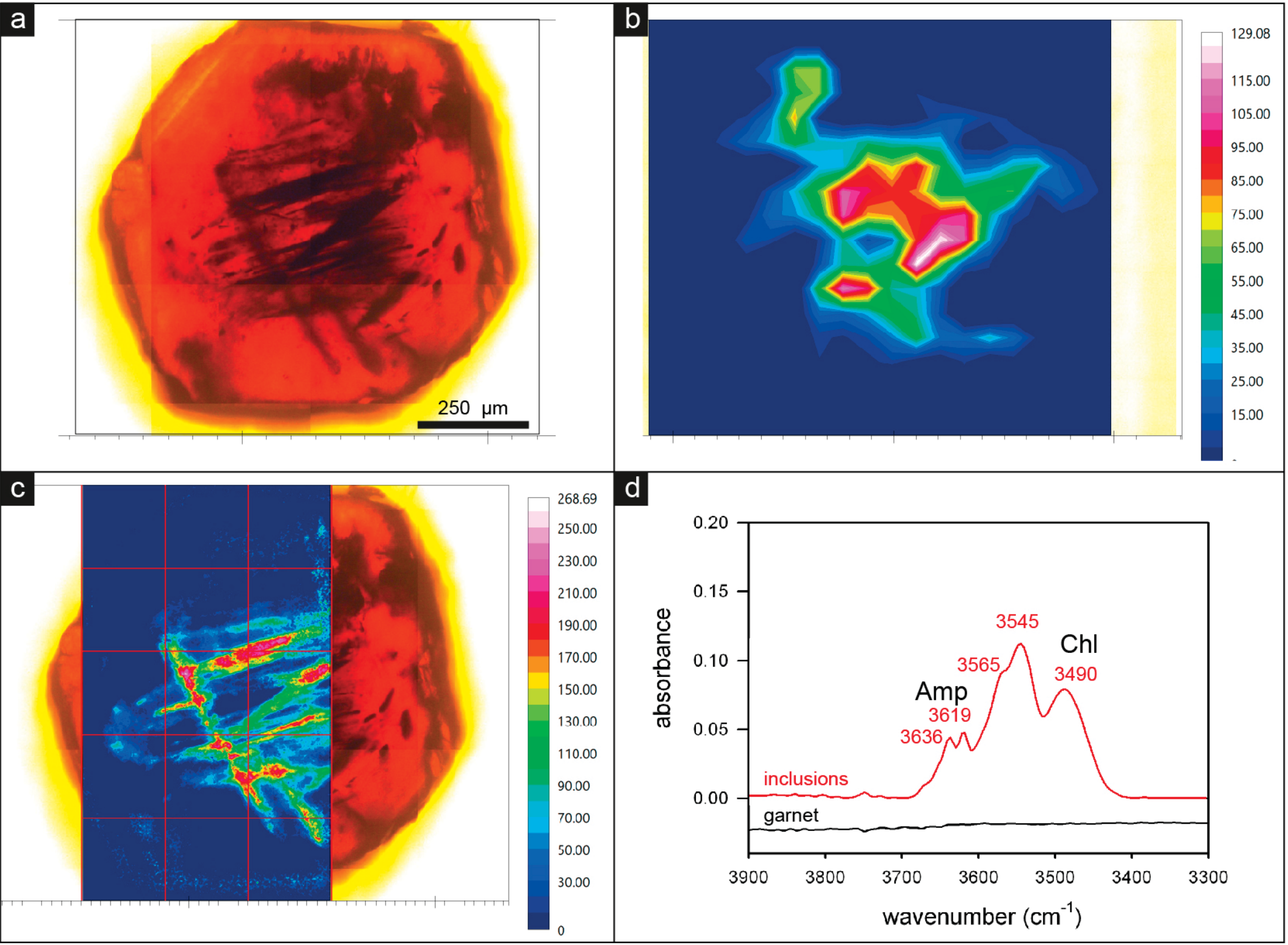
a
250 µm
b
129.08
115.00
105.00
95.00
85.00
75.00
65.00
55.00
45.00
35.00
25.00
15.00
c
268.69
250.00
230.00
210.00
190.00
170.00
150.00
130.00
110.00
90.00
70.00
50.00
30.00
0
d
absorbance
0.20
0.15
0.10
0.05
0.00
3900
3800
3700
3600
3500
3400
3300
wavenumber (cm-1)
3545
Chl
3565
3490
Amp
3619
3636
inclusions
garnet

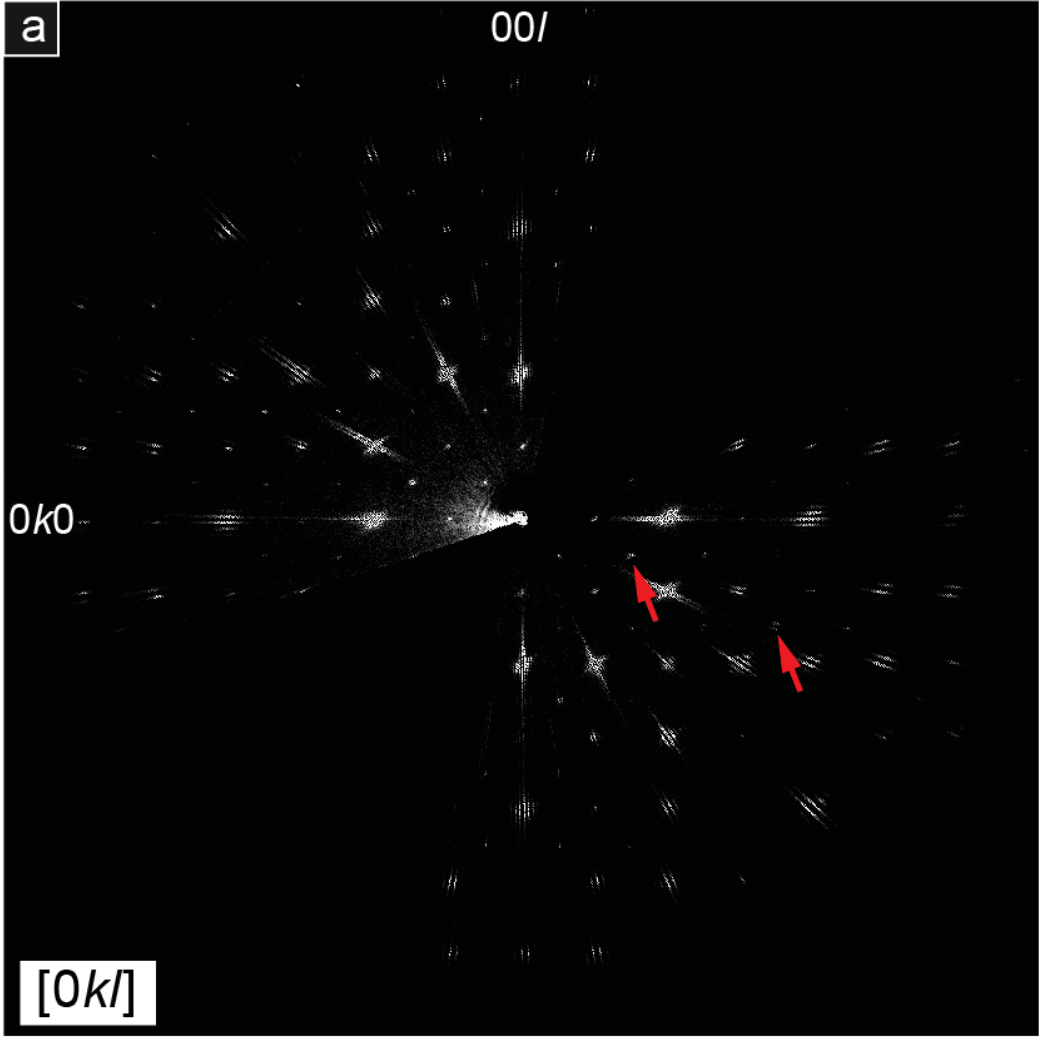
a
00l
0k0
[0kl]

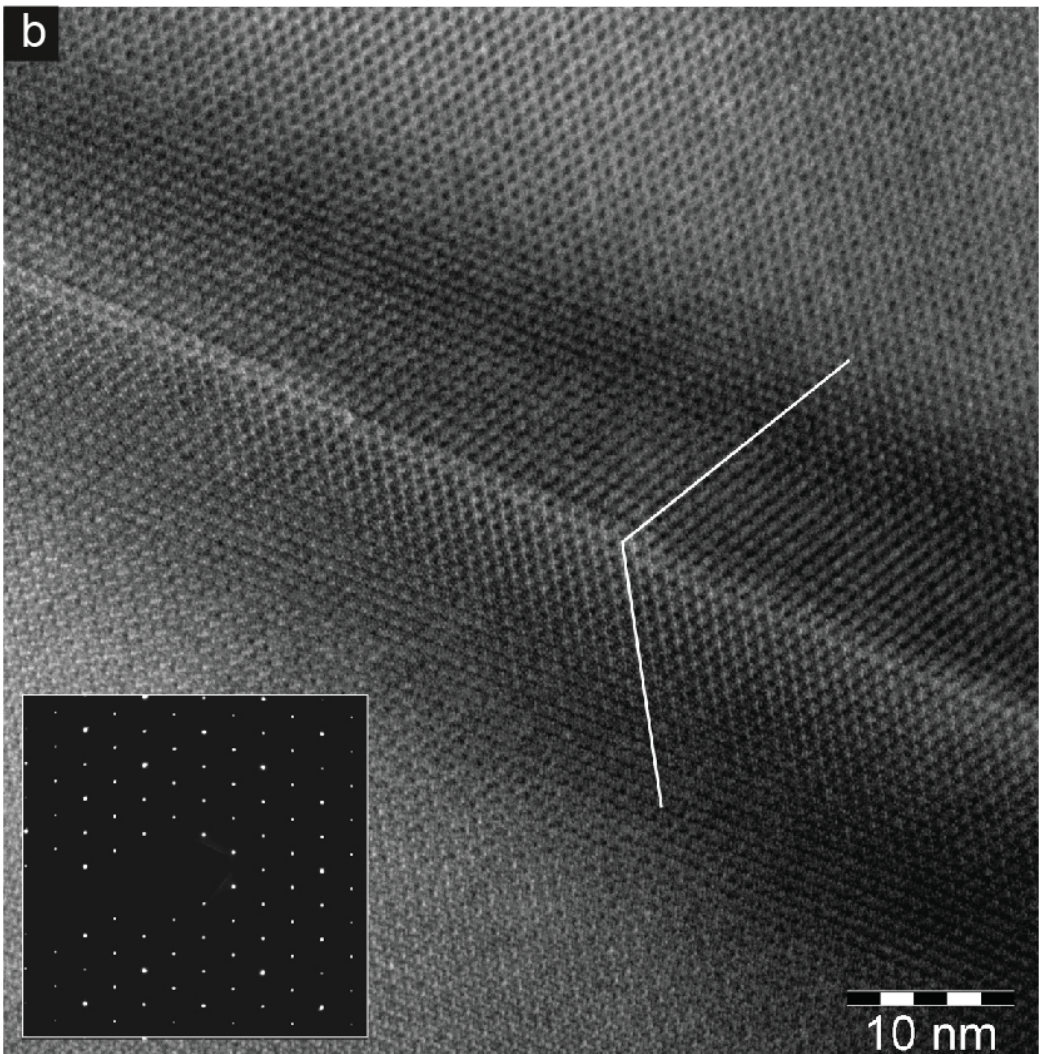
b
10 nm

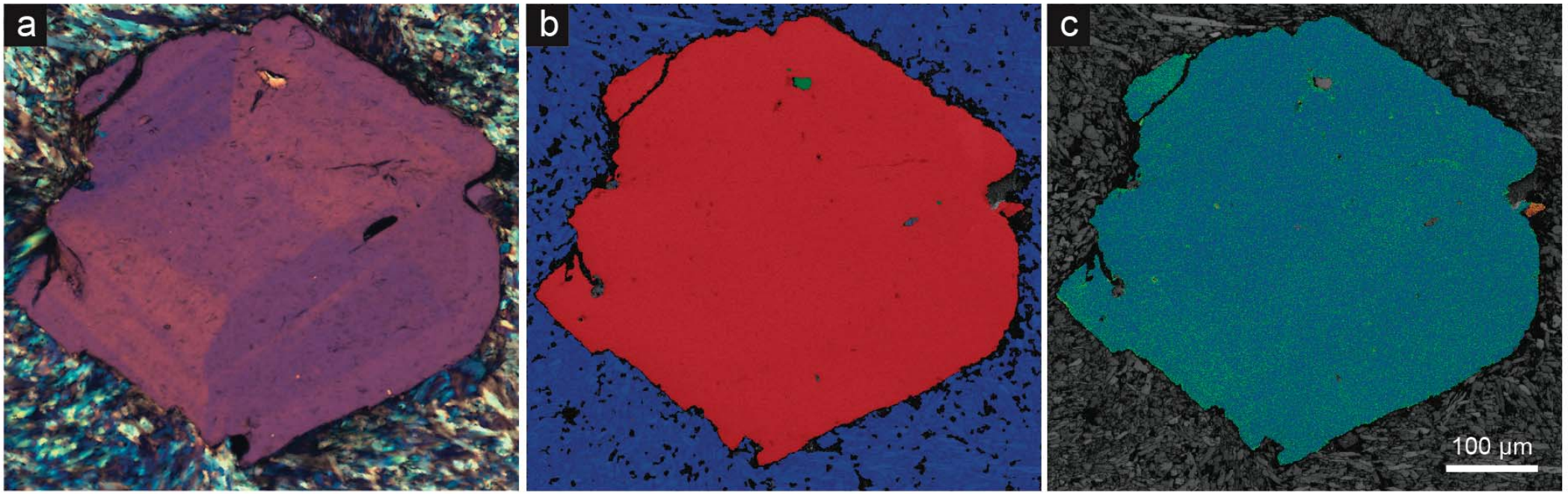
a
b
c
100 µm

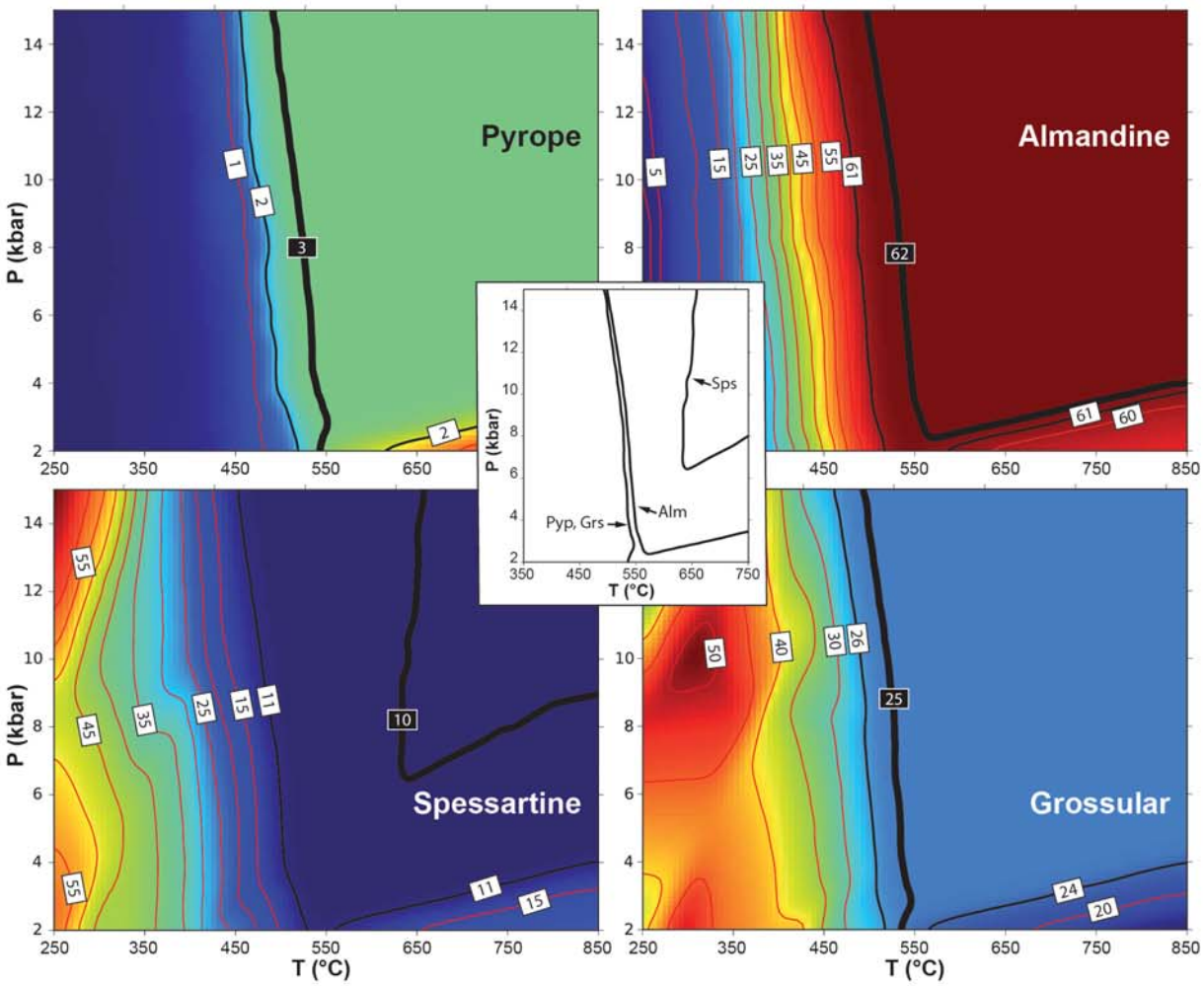
Pyrope
Almandine
Spessartine
Grossular
P (kbar)
T (°C)
Sps
Pyp, Grs
Alm